

Supplemental document for Fourier holo-ptychographic microscopy: a hybrid digital holography-Fourier ptychography approach to synthetic-aperture quantitative phase microscopy

Zhuoshi Li,^{†,‡,¶} Yefeng Shu,^{†,‡,¶} Linpeng Lu,^{†,‡,¶} Jiasong Sun,^{†,‡,¶} Qian Shen,^{†,‡,¶}
Peng Gao,^{*,§} Piotr Zdańkowski,^{||} Maciej Trusiak,^{*,||} Malgorzata Kujawinska,^{*,||}
Qian Chen,^{*,¶} and Chao Zuo^{*,†,‡,¶}

[†]*Smart Computational Imaging Laboratory (SCILab), Nanjing University of Science and
Technology, Nanjing, Jiangsu 210094, China*

[‡]*Smart Computational Imaging Research Institute (SCIRI) of Nanjing University of
Science and Technology, Nanjing, Jiangsu Province 210019, China*

[¶]*Jiangsu Key Laboratory of Spectral Imaging & Intelligent Sense, Nanjing, Jiangsu
210094, China*

[§]*School of Physics, Xidian University, Xi'an 710126, China*

^{||}*Institute of Micromechanics and Photonics, Warsaw University of Technology, 8 Sw. A.
Boboli St., Warsaw 02-525, Poland*

E-mail: peng.gao@xidian.edu.cn; maciej.trusiak@pw.edu.pl; malgorzata.kujawinska@pw.edu.pl;
chenqian@njust.edu.cn; Correspondingauthor: zuochao@njust.edu.cn

CONTENTS

1. Fourier ptychographic reconstruction in Fourier holo-ptychographic microscopy (FHPM)
2. Numerical wavefront correction algorithm in FHPM
3. Discussion on the DH initial estimate and matched-illumination condition for reliable aberration correction
4. Discussion on data redundancy requirements in FHPM with and without the DH initial estimate
5. Quantitative comparison and analysis through simulation
6. Optical transfer function analysis in FPM and diverse initial estimate schemes comparison
7. Comparison of phase recovery on buccal epithelial cells by FHPM with and without aberration correction

Supplementary Video

1. Fourier ptychographic reconstruction in Fourier holographic ptychographic microscopy (FHPM)

In Fourier ptychographic microscopy (FPM), the phase retrieval problem typically has a non-convex nature, that is, few provable global convergences guarantee exist even under ideal (noise-free) conditions. Herein, we introduce the Fourier ptychography (FP) reconstruction in FHPM, in which an adaptive step-size-based strategy is employed to ensure the stability and robustness of the reconstruction.¹ In FHPM, the low-frequency prior provided by digital holography (DH) serves as the initial estimate for the FP algorithm, yet the high-coherence light source (laser) used in DH inevitably introduces noise, which may degrade the quality and reliability of reconstruction. Although the instability problem of FP reconstruction in the presence of non-negligible noise is often attributed to the non-convex nature of phase retrieval, it is, in fact, more closely related to the choice of step size.^{2,3}

In FPM,⁴ the cost function for minimizing the amplitude error of the low-resolution image corresponding to the currently updated LED is:

$$\varepsilon = \left| \sqrt{I_j(\mathbf{r})} - \left| F^{-1}\{P(\mathbf{u})\tilde{O}(\mathbf{u} - \mathbf{u}_j)\} \right| \right|^2, \quad (\text{S1})$$

where $I_j(\mathbf{r})$ represents the captured low-resolution intensity image corresponding to the j th LED, \mathbf{r} is 2D spatial coordinate $\mathbf{r} = (x, y)$. $\tilde{O}(\mathbf{u})$ is the Fourier transform (FT) of the complex transmittance function $O(\mathbf{r})$, where $\mathbf{u} = (u, v)$ is the 2D coordinate in the Fourier space and $\mathbf{u}_j = (u_j, v_j)$ is spatial frequency coordinate corresponding to each tilted illumination angle. $P(\mathbf{u})$ is the pupil function. Theoretically, in the incremental optimal model,⁴ cost function ε cannot promise to converge to the global optimal solution and is susceptible to noise. However, its fast convergence rate and high convergence accuracy under low noise conditions make it well-suited for FP reconstruction. To minimize ε , the gradient descent method is adopted for solving the global optimum, and the updating formula of specimen spectrum is

given as follows:

$$\tilde{O}(\mathbf{u} - \mathbf{u}_j) = \tilde{O}(\mathbf{u} - \mathbf{u}_j) + \alpha^k \frac{|P(\mathbf{u})|^2}{|P(\mathbf{u})|_{\max}^2} \frac{P^*(\mathbf{u})}{|P(\mathbf{u})|^2 + \delta} [\tilde{O}_j^u(\mathbf{u}) - \tilde{O}_j^e(\mathbf{u})], \quad (\text{S2})$$

where $\tilde{O}_j^u(\mathbf{u})$ and $\tilde{O}_j^e(\mathbf{u})$ are the Fourier spectrum with and without the amplitude constraint respectively, and α is the updating step size. δ is the regularization parameter. In Eq. S2, the choice of the step-size α plays an important role for the success of FP reconstruction. A constant step-size with a larger value can achieve fast convergence at the early stage, yet it typically makes the algorithm strongly oscillatory in the neighborhood of a solution and thus may not converge to a stationary point. On the other hand, for constant but sufficiently small α , the stability of convergence is improved, but the speed of convergence is limited. Therefore, the adaptive step-size strategy is adopted to guarantee faster convergence rate while preventing falling into a local optimum. The specific step-size update condition is:

$$\alpha^{k+1} = \begin{cases} \alpha^k & , \frac{\varepsilon^{k-1} - \varepsilon^k}{\varepsilon^{k-1}} > 0.01 \\ \alpha^k / 2 & , \text{else}, \end{cases} \quad (\text{S3})$$

$$\varepsilon^k = \sum_j \left| \sqrt{I_j(\mathbf{r})} - \left| F^{-1}\{P(\mathbf{u})\tilde{O}(\mathbf{u} - \mathbf{u}_j)\} \right| \right|^2. \quad (\text{S4})$$

When the incremental gradient iteration coefficient α^k is less than a given threshold (recommended value is 0.001), stop the iteration. The complete algorithmic procedure is provided by Algorithm S1. It should be noted that the adaptive step-size-based FP reconstruction algorithm introduced here provides significant enhancements over the constant step-size strategy in terms of convergence rate and reconstruction accuracy. Although the initial estimate reconstructed from a hologram inevitably contains speckle noise due to using a high-coherent source in DH part of FHPM, the adopted adaptive step-size strategy can still guarantee accurate and reliable convergence. Meanwhile, the high-signal-to-noise ratio (SNR) intensity images collected with LED illumination are iteratively incorporated in the Fourier space,

thereby averaging out the speckle noise and improving the imaging quality.

Algorithm S1 Adaptive step-size-based Fourier ptychographic reconstruction algorithm in FHPM for phase recovery and aberration characterization

Require: one hologram with on-axis illumination $I_H(\mathbf{r})$; eight intensity images with angle-varied illumination $I_j(\mathbf{r})$; the pupil function $P(\mathbf{u})$.

- 1: Reconstruct the complex field $U_H(\mathbf{r})$ from $I_H(\mathbf{r})$.
 - 2: Fill the central aperture in the Fourier space for initial estimate $\tilde{O}(\mathbf{u}) = F\{U_H(\mathbf{r})\}$.
 - 3: set $k \in \{1 \dots K\}$, $\varepsilon^0 = 0$, and $\alpha^1 = 1$
 - 4: **repeat**
 - 5: **for** $j \in \{1 \dots 8\}$ **do**
 - 6: $\tilde{O}(\mathbf{u} - \mathbf{u}_j) = \tilde{O}(\mathbf{u} - \mathbf{u}_j) + \alpha^k \frac{|P(\mathbf{u})|^2}{|P(\mathbf{u})|_{\max}^2} \frac{P^*(\mathbf{u})}{|P(\mathbf{u})|^2 + \delta} [\tilde{O}_j^u(\mathbf{u}) - \tilde{O}_j^e(\mathbf{u})]$
 - 7: $P(\mathbf{u}) = \text{circ}(\frac{\sqrt{\mathbf{u}^2}}{NA/\lambda}) \exp(i \sum_n^{21} k_n Z_n(\mathbf{u}))$
 - 8: $\varepsilon^k = \sum_j \left| \sqrt{I_j(\mathbf{r})} - \left| F^{-1}\{P(\mathbf{u})\tilde{O}(\mathbf{u} - \mathbf{u}_j)\} \right| \right|^2$
 - 9: **end for**
 - 10: **if** $(\varepsilon^{k-1} - \varepsilon^k)/\varepsilon^k > 0.01$ **then**
 - 11: $\alpha^{k+1} = \alpha^k$
 - 12: **else**
 - 13: $\alpha^{k+1} = \alpha^k/2$
 - 14: **end if**
 - 15: **until** $\alpha^k < 0.001$
 - 16: **return** $U(\mathbf{r}) = F^{-1}\{\tilde{O}(\mathbf{u})\}$ and $P(\mathbf{u})$
-

2. Numerical wavefront correction algorithm in FHPM

In realistic scenarios, mechanical perturbations and thermal fluctuations of the microscopy, as well as optically inhomogeneous structure of biological specimens will result in imaging aberrations, significantly degrading the imaging contrast and quality. Here, we introduce a numerical wavefront correction algorithm based on Zernike mode constraint adopted in FHPM. In Section 1, the presented FP reconstruction process is fundamentally derived from the enhanced ptychographic iterative engine (ePIE),⁵ and the updating process for the specimen spectrum is given as Eq. S2. Similarly, the pupil function can be reconstructed in an analogous way as shown in Eq. S5, where the pupil function and the spectrum are

reversed.

$$P(\mathbf{u}) = P(\mathbf{u}) + \beta \frac{O^*(\mathbf{u} - \mathbf{u}_j)}{|O(\mathbf{u} - \mathbf{u}_j)|^2 + \gamma} [\tilde{O}_j^u(\mathbf{u}) - \tilde{O}_j^e(\mathbf{u})], \quad (\text{S5})$$

where β is the pupil updating step size, γ is the regularization parameter. Notably, unlike pupil updating formula proposed in EPRY, Eq. S5 omits the normalized spectrum modulus.⁶ In practical implementation, Eq. S2 and Eq. S5 are applied to alternatively update the object function and the pupil function until the convergence condition is satisfied. However, the joint estimation of both the object and pupil enhances the degree of ill-posedness of the inverse problem. Therefore, in the numerical wavefront correction strategy used in FHPM, we employed Zernike polynomials as prior knowledge for aberration characterization, and utilized them as a suitable basis to express pupil aberration,^{7,8}

$$P(\mathbf{u}) = \text{circ}\left(\frac{\sqrt{\mathbf{u}^2}}{NA/\lambda}\right) \exp(i \sum_n^{21} k_n Z_n(\mathbf{u})), \quad (\text{S6})$$

where $\text{circ}(\frac{\sqrt{\mathbf{u}^2}}{NA/\lambda})$ denotes a low-pass filter with a radius of NA/λ . The aberration term is characterized by $\sum_n^{21} k_n Z_n(\mathbf{u})$, in which k_n is the weight coefficient and $Z_n(\mathbf{u})$ is the n th Zernike polynomial. Hence, the degrees of freedom in solution space are reduced from a two-dimensional matrix to a small set of coefficients associated with the dominant Zernike modes. Even though the numerical wavefront correction approach introduced here is somewhat similar to the algorithm proposed in AO-QPI,⁹ in fact, it is a further application of AO-QPI. In FHPM, the wavefront aberrations are coupled not only into the intensity images but also into the complex amplitude and modulated in a hologram. Consequently, we initially reconstruct the aberration together with the Zernike mode constraint (Eq. S6), and correct the DH complex amplitude using the results of initial estimation. Thereafter, the aberration characterization is performed again utilizing the corrected DH complex amplitude as low-frequency prior (*i.e.*, repeating the above process), and the accurate wavefront aberrations are finally recovered.

3. Discussion on the DH initial estimate and matched-illumination condition for reliable aberration correction

In this section, we discuss the significance of the accurate initial estimate (low-frequency prior) provided by DH for reliable aberration recovery, especially when the matched-illumination condition is not properly fulfilled. Here, we perform the simulation of aberration recovery with the input aberration in Fig. S1(a1) and input specimen phases in Figs. S1(a2) and (a3). Two kinds of specimens as the input phase (an object containing only low-frequency features and a complicated object containing both low- and high- frequency) are adopted in the experiment, which is because the frequency characteristic of the specimen is a non-negligible factor that could affect the accuracy of aberration characterization. To verify the effect of the DH initial estimate and matched-illumination condition for aberration correction, we perform simulations using the same number of intensity images (8 intensity images), but with different LED tilted illumination angles [$NA_{ill} = NA_{obj}, 0.75NA_{obj}, 0.5NA_{obj}$, as shown in Figs. S1(b1-b3)], and with or without center laser illumination [see Figs. S1(b4-b5)]. The reconstructed aberrations and convergence curves are presented in Figs. S1(c1-c5), (d1-d5), and (e-f). It can be seen that the aberrations are accurately characterized under the matched-illumination condition. While if the adopted illumination angle gets smaller than objective numerical aperture (NA), the reconstructed aberrations tend to be unreliable, and the algorithm cannot also converge to the correct solution. However, as presented in Figs. S1(c4-c5) and (d4-d5), due to the accurate low-frequency prior reconstructed by DH, FHPM not only ensures the accuracy of phase recovery but also aberration characterization, even when the matched-illumination condition cannot be strictly satisfied. This feature makes the proposed method bypass the difficulty of tuning the illumination angle to match the objective NA, which is very important in practical imaging setups, especially when using a high-NA objective lens (*e.g.*, an oil-immersion objective lens) in a microscopic system.

In addition, it should be noted that the aberrations are reconstructed more accurately

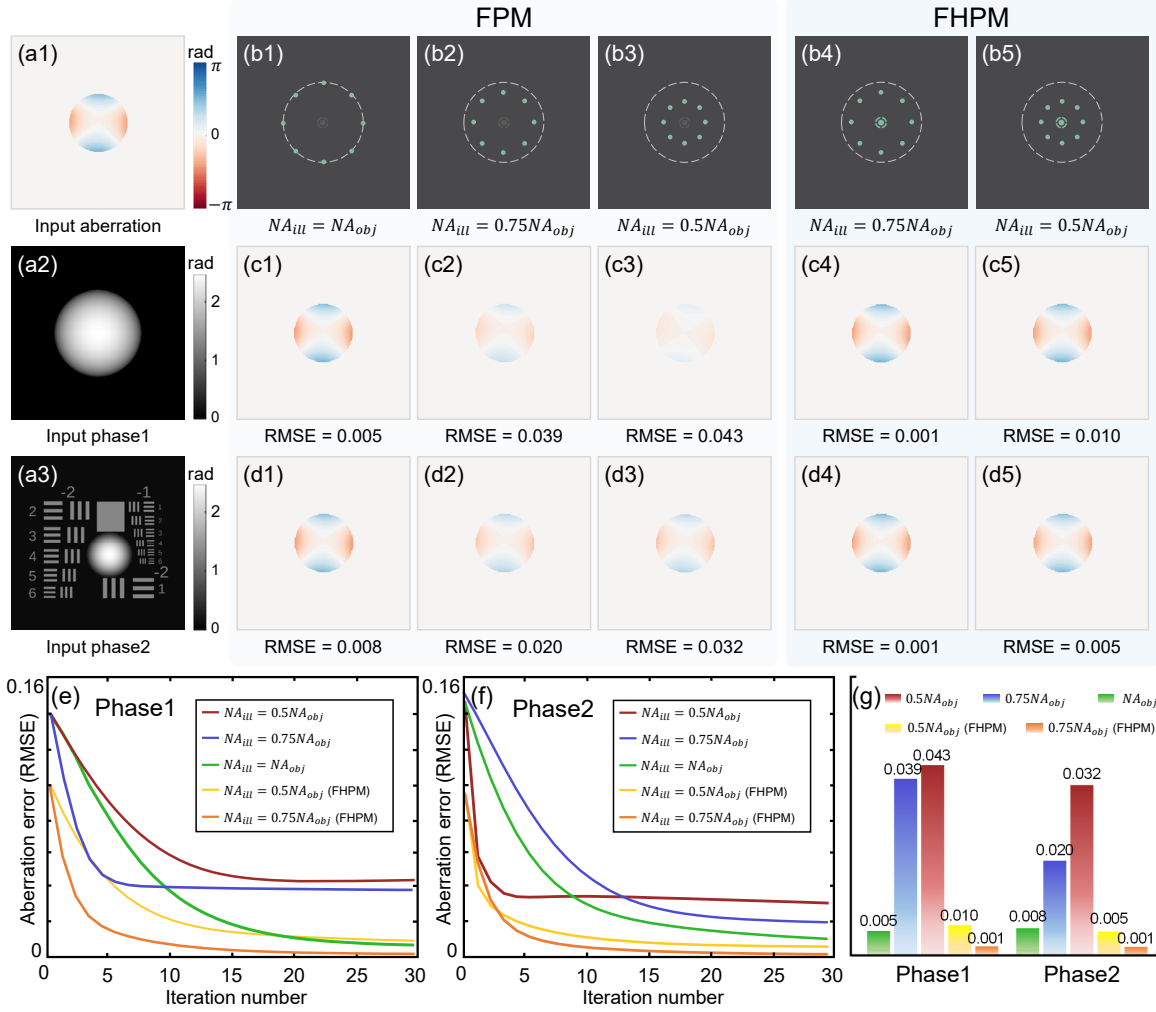


Figure S1: Comparison of the reconstructed results under annular illumination of different angles with and without the initial estimate provided by DH. (a1-a3) The input specimen aberration and input phases for the simulation. (b1-b5) The annular illumination modes of the LED with different angles, where the laser is lit up in (b4-b5) to obtain the accurate low frequency. (c1-c5) and (d1-d5) The reconstructed aberrations corresponding to the different illumination modes in (b1-b5) with input phase 1 and 2, respectively. (e) and (f) The convergence curves of the aberration error. (g) The histogram distribution of the recovered aberration error.

with the complicated specimen (input phase 2) that contains some high-frequency information under the same non-matched illumination, as shown in Figs. S1(c2-c3) and (d2-d3). However, for low-frequency phase object such as microlens array (input phase 1), the aberration is completely underestimated. This is because, according to the phase transfer function analysis of FPM (specific discussion is also provided in Section 6),¹⁰ the low-frequency phase information is missing under non-matched illumination, and the object phase and the wavefront aberrations are inseparably coupled into the intensity images.⁹ Hence, there is almost no information of the aberrations being transferred into the intensity contrast for low-frequency phase specimens. In contrast, due to the accurate low-frequency initial estimate provided by DH, FHPM can secure the accuracy of aberration reconstruction for multiple types of specimens (containing low- or high- frequency phase components) without stringent matched-illumination condition, demonstrating better feasibility and practicality. Furthermore, Fig. S1(g) provides a histogram distribution to compare the experimental results, which more explicitly indicates that FHPM can accurately recover wavefront aberrations for any samples under various system parameters (even using a high-NA objective lens in a microscopic system). However, in sophisticated experimental scenarios, the phase reconstruction quality is typically plagued by the dynamically varying aberrations. The low-frequency prior provided by DHM in FHPM also facilitates accurate and robust aberration characterization under non-matched illumination, while FPM exhibits limited performance, as animated in Visualization 2.

4. Discussion on data redundancy requirements in FHPM with and without the DH initial estimate

In FPM, simultaneously recovering phase and aberration is a typical ill-posed inverse problem, and solving this problem typically adopts a non-linear optimization approach. Therefore, the correctness of the solution highly depends on the data redundancy.^{11–13} Here, we

discuss the data redundancy requirements for the proper solution of the non-linear optimization problem in FHPM with and without low-frequency initial estimate provided by DH. Generally, at least 35% aperture overlapping ratio in the Fourier domain is required for a successful reconstruction using FPM.¹² Hence, we used 4, 6, 8, 12, and 24 intensity images for phase recovery ($N = 4, 6, 8, 12, 24$), corresponding to aperture overlapping ratios of 18.15%, 39.14%, 58.14%, 67.94%, and 75.13% (with a $20\times$, 0.5NA objective lens, and a pixel size of $4.4\ \mu\text{m}$, $NA_{ill} = 0.95NA_{obj}$), and their spectra are shown in Figs. S2(d1-h1). The hologram and intensity images used are presented in Fig. S2(a). Figures S2(d2-h2) showcase phase reconstruction results using FHPM, respectively, and the error distributions are depicted in Figs. S2(d3-h3), on which the RMSE values relative to the ground truth (GT) are located at the top. It can be seen that the phase reconstruction accuracy will not improve further when the number of intensity images used exceeds 8. The varying numerical curve [as shown in Fig. S2(b)] of the phase reconstruction error with different intensity images numbers N can more intuitively draw this conclusion. Theoretically, the successful phase reconstruction in FPM using 6 intensity images (39.14% overlapping ratios) is sufficient. Whereas, recovering phase while reconstructing aberration increases the difficulty of solving ill-posed inverse problems. Figures S2(d4-h4) present the quantitative profile results of Group -1 to demonstrate the high-frequency phase reconstruction performance with varying number of intensity images.

In addition, it should be noted that the FP algorithm without the DH initial estimate can only converge stably when at least 12 intensity images are used, as illustrated in Figs. S2(c) and (d5-h5). However, only 8 intensity images are sufficient in FHPM. This occurs because the low-frequency prior fills the central aperture in the Fourier space, which improves the aperture overlapping ratio, reducing the difficulty of convergence. Therefore, the accurate low-frequency initial estimate provided by DH not only ensures the accuracy of phase recovery and aberration characterization, but also relieve the data redundancy requirement for a successful ptychographic reconstruction.

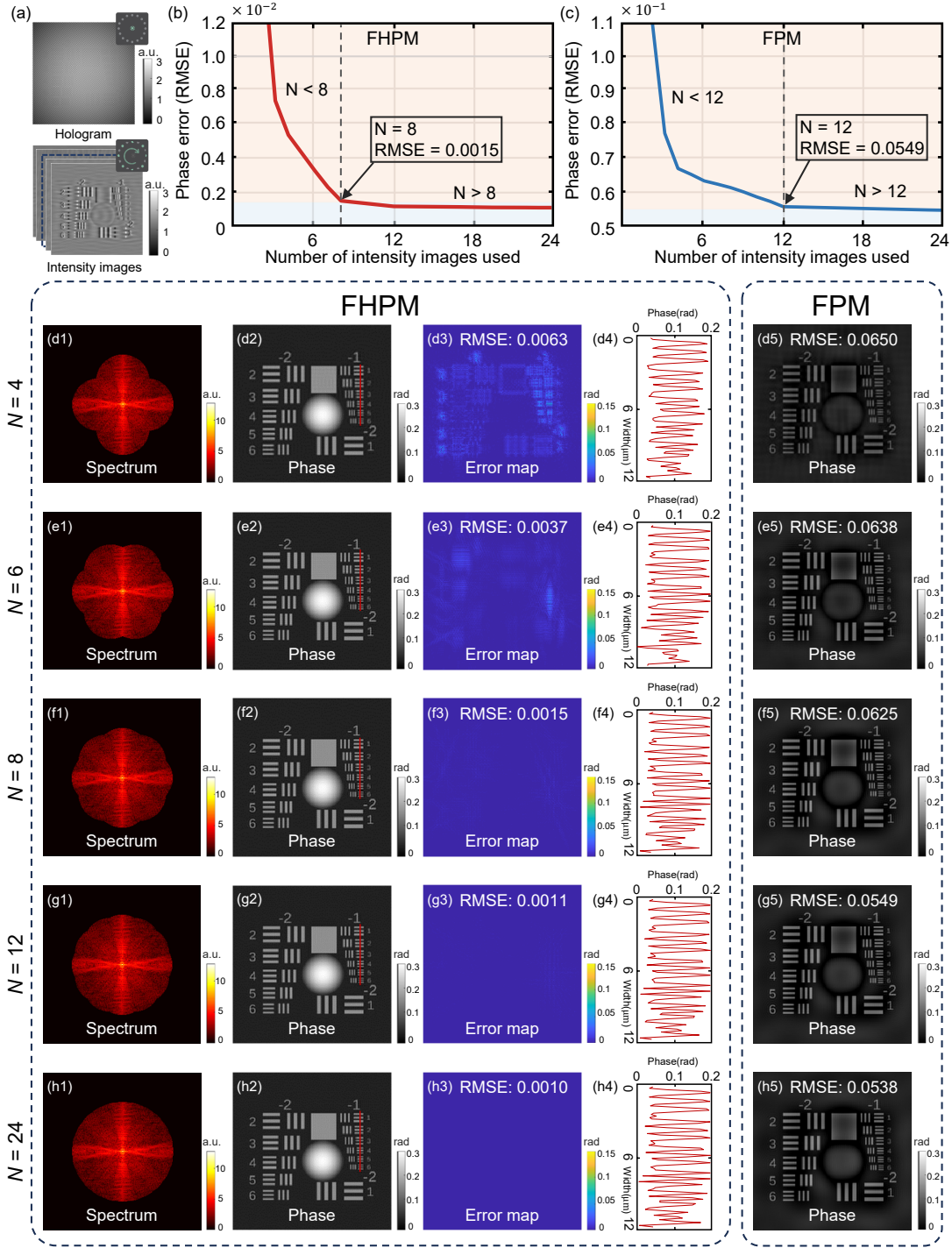


Figure S2: Simulation results of phase reconstruction error with different numbers of intensity images used. (a) The hologram and intensity images used. (b) and (c) The variation curve of phase error with the number of intensity images used. (d1-h1) The spectra corresponding to different numbers of intensity images. (d2-h2) The phase recovery results by FHPM using different numbers of intensity images, and (d3-h3) are the error distribution maps. (d4-h4) The line profiles cross Group -1 of (d2-h2). (d5-h5) The phase recovery results by FPM using different numbers of intensity images.

5. Quantitative comparison and analysis through simulation

In this section, we performed simulation under 532 *nm* wavelength laser/LED illumination with a 4.4 μm pixel size detector and the 20 \times , 0.5NA objective lens (mirroring the parameters of our actual experimental system) to verify the reasonableness of the proposed FHPM platform and the feasibility of the hybrid DH and FP approach. Meanwhile, we set the tilted illumination angle to render the illumination NA close to the objective NA for simulating the realistic proximity to the matched-illumination scenario ($NA_{ill} = 0.95NA_{obj}$), since perfectly matched illumination is not a trivial task in actual configuration. Figures S3(a-c) respectively show the QPI results by DHM, FPM, and FHPM with their corresponding spectra in the bottom right corner, where DHM exhibits the limited imaging resolution, as illustrated by the quantitative profile in Fig. S3(i). FPM enables a higher resolution, yet as indicated by the error map in Fig. S3(f), the low-frequency phase, especially within the circular region, is notably absent. In contrast, FHPM achieves high-resolution imaging while ensuring the accuracy of phase reconstruction, closely mirroring the GT [Fig. S3(d)], as depicted in the error distributions in Figs. S3(e-g). The line profile across the circular region [Fig. S3(h)] quantitatively indicates that the phase value recovered by FHPM is in good agreement with the GT, whereas FPM demonstrates obvious low-frequency phase missing. Furthermore, We selected a rectangular region and calculated the histograms of the dashed box regions of Figs. S3(a-c), as shown in Fig. S3(j). The histograms provide a direct visualization of the phase distribution, further demonstrating the effectiveness of the proposed method for accurate phase reconstruction.

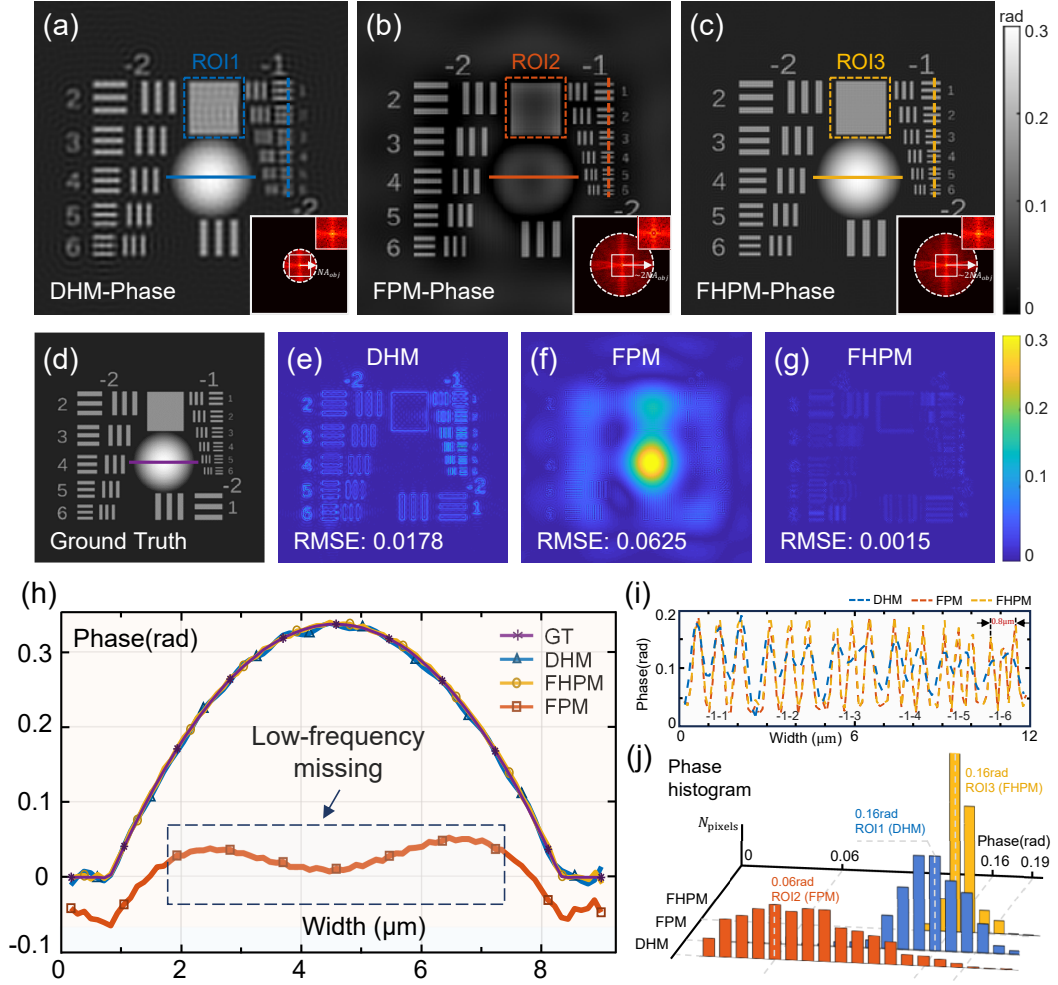


Figure S3: Quantitative simulation results with the different imaging methods. (a-c) Quantitative phase imaging results of DHM, FPM, and FHPM, respectively. (d) Ground truth. (e-g) Error distribution maps of the phase recovery results of three methods relative to ground truth. (h) The line profile across the circular region in (a), (b), and (c), in which the blue box underscores the incorrect low-frequency phase recovery of FPM. (i) Quantitative profile of the phase imaging results by three methods, corresponding to (a-c), respectively. (j) Phase histogram of the boxed regions in (a-c).

6. Optical transfer function analysis in FPM and diverse initial estimate schemes comparison

To further emphasize the significance of the initial estimate for FPM, in this section, we analyze the optical transfer function (OTF) of FPM and compare the phase reconstruction results using different initial estimates. Unlike DHM, which encodes and decodes the complete complex amplitude of object interferometrically, and differential phase contrast (DPC),^{14–16} which directly retrieves the phase through two-dimensional deconvolution, FPM iteratively reconstructs the sample's complex amplitude distribution based on intensity-only measurements with tilted illuminations. Herein, we analyze the OTF of FPM to quantify how phase information is converted into intensity and reveal the phase measuring accuracy for FPM. Consider a weak object with a complex transmission function:

$$\begin{aligned} O(\mathbf{r}) &= \sqrt{I_{obj}(\mathbf{r})} \exp(i\varphi(\mathbf{r})) = \sqrt{\exp(a(\mathbf{r}))} \exp(i\varphi(\mathbf{r})) \\ &= \exp(\frac{1}{2}a(\mathbf{r}) + i\varphi(\mathbf{r})) \approx 1 + \frac{1}{2}a(\mathbf{r}) + i\varphi(\mathbf{r}) \end{aligned} \quad (S7)$$

where $O(\mathbf{r})$ is the complex amplitude of the object, $I_{obj}(\mathbf{r})$ and $\varphi(\mathbf{r})$ present its intensity and phase distributions. To facilitate analysis, we define the absorption distribution of the object as $I_{obj}(\mathbf{r}) = \exp(a(\mathbf{r}))$ and adopt a weak object approximation.^{17,18} We take the Fourier transform on both sides of Eq. S7 and obtain the Fourier spectrum of $O(\mathbf{r})$ to analyze the transfer function:

$$\tilde{O}(\mathbf{u}) = \delta(\mathbf{u}) + \frac{1}{2}A(\mathbf{u}) + i\Phi(\mathbf{u}), \quad (S8)$$

where $\delta(\mathbf{u})$ is a Dirac Delta function, $A(\mathbf{u})$ and $\Phi(\mathbf{u})$ present the spectrum of absorption and phase distributions. When the object is illuminated by a titled plane wave, the spectrum will be shifted in the Fourier space. Thus, the Fourier spectrum of the transmitted complex

wave-front with the tilted illumination angle $\mathbf{u}_0 = (u_0, v_0)$ can be formulated as:

$$W_{obj}(\mathbf{u}) = \tilde{O}(\mathbf{u} - \mathbf{u}_0) = \delta(\mathbf{u} - \mathbf{u}_0) + \frac{1}{2}A(\mathbf{u} - \mathbf{u}_0) + i\Phi(\mathbf{u} - \mathbf{u}_0), \quad (\text{S9})$$

The complex wave-front is low-pass filtered by the pupil function $P(\mathbf{u})$ in the Fourier domain before reaching the camera.

$$W_{cam}(\mathbf{u}) = W_{obj}(\mathbf{u})P(\mathbf{u}), \quad (\text{S10})$$

Assuming that $P(\mathbf{u})$ is an ideal low pass filter with the cut-off frequency of NA_{obj}/λ , the complex wave-front spectrum at the imaging plane is:

$$W_{cam}(\mathbf{u}) = \begin{cases} \delta(\mathbf{u} - \mathbf{u}_0) + \frac{1}{2}A(\mathbf{u} - \mathbf{u}_0)P(\mathbf{u}) + i\Phi(\mathbf{u} - \mathbf{u}_0)P(\mathbf{u}), & |\mathbf{u}_0| \leq \frac{NA_{obj}}{\lambda} \\ \frac{1}{2}A(\mathbf{u} - \mathbf{u}_0)P(\mathbf{u}) + i\Phi(\mathbf{u} - \mathbf{u}_0)P(\mathbf{u}), & else \end{cases}, \quad (\text{S11})$$

where $|\mathbf{u}_0| \leq NA_{obj}/\lambda$ denotes the bright-field imaging condition when illumination NA is not larger than objective NA. By calculating the convolution process between $W_{cam}(\mathbf{u})$ and its complex conjugate $W'_{cam}(\mathbf{u})$, we can gain the intensity spectrum for bright-field imaging in FPM as:

$$\begin{aligned} I_{cam}(\mathbf{u}) &= W_{cam}(\mathbf{u}) * W'_{cam}(\mathbf{u}) \\ &\approx \delta(\mathbf{u}) + \frac{1}{2}A(\mathbf{u})[P(\mathbf{u} + \mathbf{u}_0) + P(\mathbf{u} - \mathbf{u}_0)] + i\Phi(\mathbf{u})[P(\mathbf{u} + \mathbf{u}_0) - P(\mathbf{u} - \mathbf{u}_0)] \end{aligned} \quad (\text{S12})$$

Here, we neglect the high-order convolution terms between $A(\mathbf{u})$ and $\Phi(\mathbf{u})$ for linearization.^{17,18} According to Eq. S12, the intensity spectrum can be separated into three terms: background term, absorption transfer term, and phase transfer term. Thus, the amplitude transfer function (ATF) and phase transfer function (PTF) for bright-field imaging of a weak object in FPM can be represented as:

$$ATF(\mathbf{u}) = \frac{1}{2}[P(\mathbf{u} + \mathbf{u}_0) + P(\mathbf{u} - \mathbf{u}_0)] \quad (\text{S13})$$

$$PTF(\mathbf{u}) = i[P(\mathbf{u} + \mathbf{u}_0) - P(\mathbf{u} - \mathbf{u}_0)]. \quad (\text{S14})$$

It is evident that the complete phase information can be transferred to the intensity images only under matched illumination ($NA_{obj} = NA_{ill}$), otherwise, the low-frequency part will be missed. Figures S4(a-c) showcase the PTF distributions in FPM (with $NA_{ill} = NA_{obj}, 0.96NA_{obj}, 0.6NA_{obj}$). However, due to the non-negligible size of the LED emitting surface ($\sim 1 \text{ mm}$) and the distribution bias of the ring-arranged LED array in the setup, the intensity images at certain illumination angles will be dark-field images as the illumination NA improves, making it quite difficult to satisfy the matched-illumination condition. Here,

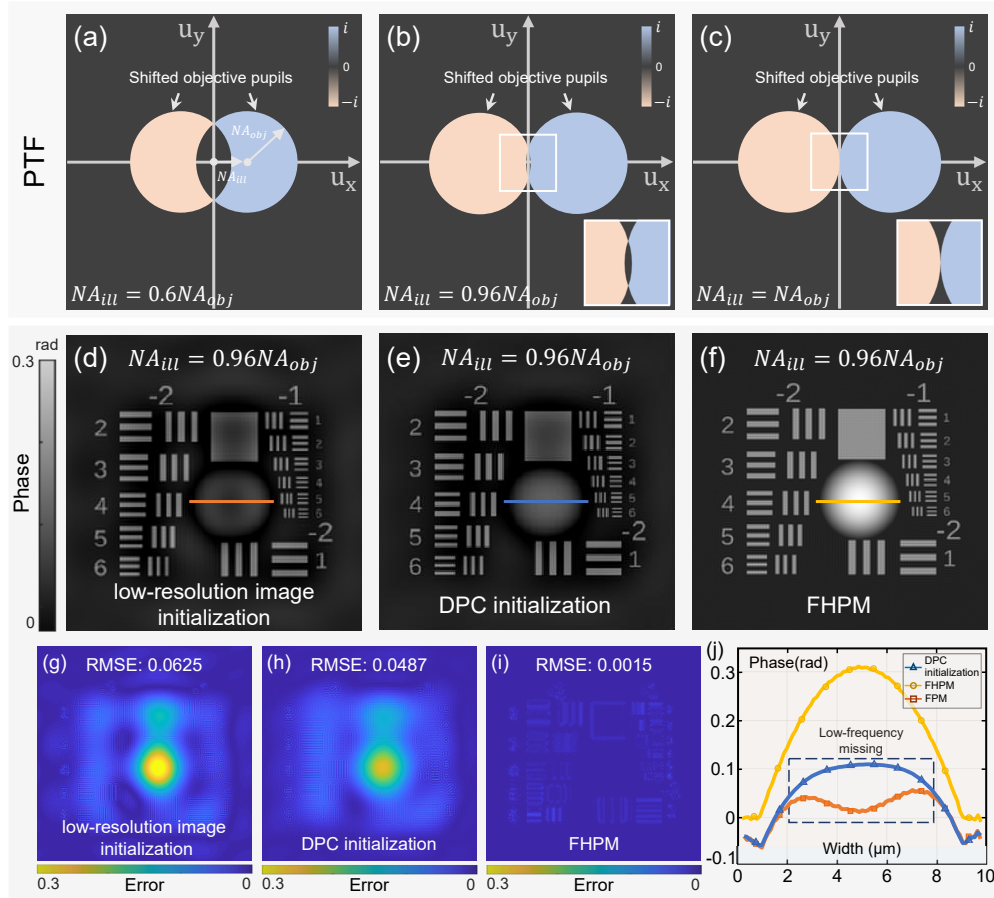


Figure S4: PTF analysis in FPM and phase reconstruction comparison with different initial estimates. (a-c) The PTFs at $NA_{ill} = 0.6NA_{obj}, 0.96NA_{obj}, NA_{obj}$. (d-f) The phase reconstruction results based on three different initialization conditions (low-resolution intensity image, DPC, and DHM) at $NA_{ill} = 0.96NA_{obj}$. (g-i) The corresponding error distribution maps. (j) The line profile across the circular area in (d-f).

we calculate a low-resolution initialization based on DPC for FP reconstruction. The four bright-field images (corresponding to the left, right, top, and bottom half-circles on the LED array) are directly used in the deconvolution-based DPC algorithm to retrieve phase information. Figures S4(d-f) provide the comparative results of FP reconstruction based on three different initialization conditions (low-resolution intensity image, DPC, and DHM) at $NA_{ill} = 0.96NA_{obj}$ (non-ideal matched-illumination condition), and the error distributions are shown in Figs. S4(g-i). It can be observed that, although FP reconstruction results with DPC-based initialization slightly surpass those of traditional FPM, they still cannot ensure accurate low-frequency phase recovery, as illustrated in the line profiles of Fig. S4(j). This is because the process, which is a scheme to reconstruct the complex field from intensity images using a phase retrieval algorithm, cannot provide reliable low-frequency prior information. Conversely, DH can fully record and reconstruct the sample's complex amplitude and serve as the initial estimate, enabling FHPM to secure quantitative phase measurements even in non-ideal matched illumination situations.

7.Comparison of phase recovery on buccal epithelial cells by FHPM with and without aberration correction

To further demonstrate the significance of aberration correction, we provide comparative results on buccal epithelial cells using FHPM with and without aberration correction. Figures S5(a) and (b) show the phase reconstruction results by FHPM under aberration correction on and off, respectively. The zoomed-in views of Area 1 and Area 2 in Figs. S5(a) and (b) are shown in Figs. S5(c-f), from which the results without aberration correction are more blurring-out. From the line profiles illustrated in Figs. S5(h) and (i), it can be seen that the inner subcellular structures are more clearly resolved with accurate aberration characterization, whereas they appear relatively smoothed when the aberration correction is off. The reconstructed aberration is depicted in Fig. S5(g). These results demonstrate that accurate

wavefront aberration correction can effectively improve the quality and contrast of phase imaging, ensuring accurate and reliable observation of cell- and subcell-scale structure, permitting the potential of the FHPM approach and platform for quantitative characterization of cell morphology, which is important for many applications, such as cancer screening, stem cell research, and drug development.¹⁹

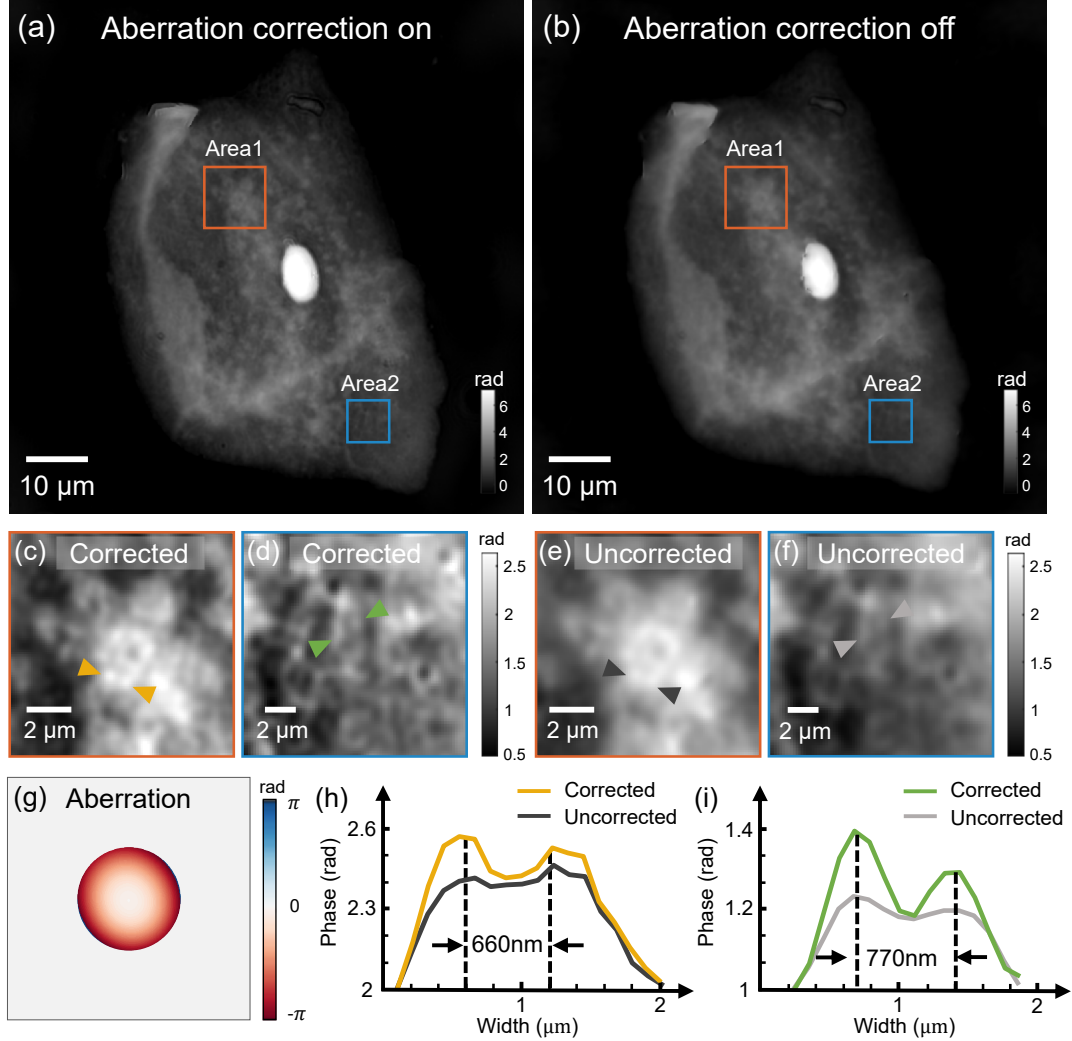


Figure S5: Comparison of phase reconstruction results on a buccal epithelial cell using FHPM with or without aberration correction. (a) and (b) The corresponding results under aberration correction on and off, respectively. (c-f) The enlarged views corresponding to the boxes in (a) and (b). (g) The reconstructed aberration. (h) and (i) The cross sections on different subcellular structures in (c-f).

References

- (1) Zuo, C.; Sun, J.; Chen, Q. Adaptive step-size strategy for noise-robust Fourier ptychographic microscopy. *Optics express* **2016**, *24*, 20724–20744.
- (2) Zhang, F.; Peterson, I.; Vila-Comamala, J.; Diaz, A.; Berenguer, F.; Bean, R.; Chen, B.; Menzel, A.; Robinson, I. K.; Rodenburg, J. M. Translation position determination in ptychographic coherent diffraction imaging. *Optics express* **2013**, *21*, 13592–13606.
- (3) Luke, D. R. Relaxed averaged alternating reflections for diffraction imaging. *Inverse problems* **2004**, *21*, 37.
- (4) Zheng, G.; Horstmeyer, R.; Yang, C. Wide-field, high-resolution Fourier ptychographic microscopy. *Nature photonics* **2013**, *7*, 739–745.
- (5) Maiden, A. M.; Rodenburg, J. M. An improved ptychographical phase retrieval algorithm for diffractive imaging. *Ultramicroscopy* **2009**, *109*, 1256–1262.
- (6) Ou, X.; Zheng, G.; Yang, C. Embedded pupil function recovery for Fourier ptychographic microscopy. *Optics express* **2014**, *22*, 4960–4972.
- (7) Song, P.; Jiang, S.; Zhang, H.; Huang, X.; Zhang, Y.; Zheng, G. Full-field Fourier ptychography (FFP): Spatially varying pupil modeling and its application for rapid field-dependent aberration metrology. *APL Photonics* **2019**, *4*.
- (8) Lakshminarayanan, V.; Fleck, A. Zernike polynomials: a guide. *Journal of Modern Optics* **2011**, *58*, 545–561.
- (9) Shu, Y.; Sun, J.; Lyu, J.; Fan, Y.; Zhou, N.; Ye, R.; Zheng, G.; Chen, Q.; Zuo, C. Adaptive optical quantitative phase imaging based on annular illumination Fourier ptychographic microscopy. *Photonix* **2022**, *3*, 24.

- (10) Sun, J.; Zuo, C.; Zhang, J.; Fan, Y.; Chen, Q. High-speed Fourier ptychographic microscopy based on programmable annular illuminations. *Scientific reports* **2018**, *8*, 7669.
- (11) Dong, S.; Bian, Z.; Shiradkar, R.; Zheng, G. Sparsely sampled Fourier ptychography. *Optics express* **2014**, *22*, 5455–5464.
- (12) Sun, J.; Chen, Q.; Zhang, Y.; Zuo, C. Sampling criteria for Fourier ptychographic microscopy in object space and frequency space. *Optics express* **2016**, *24*, 15765–15781.
- (13) Fan, Y.; Sun, J.; Shu, Y.; Zhang, Z.; Zheng, G.; Chen, W.; Zhang, J.; Gui, K.; Wang, K.; Chen, Q.; others Efficient synthetic aperture for phaseless Fourier ptychographic microscopy with hybrid coherent and incoherent illumination. *Laser & Photonics Reviews* **2023**, *17*, 2200201.
- (14) Tian, L.; Waller, L. Quantitative differential phase contrast imaging in an LED array microscope. *Optics express* **2015**, *23*, 11394–11403.
- (15) Fan, Y.; Sun, J.; Chen, Q.; Pan, X.; Tian, L.; Zuo, C. Optimal illumination scheme for isotropic quantitative differential phase contrast microscopy. *Photonics Research* **2019**, *7*, 890–904.
- (16) Fan, Y.; Sun, J.; Shu, Y.; Zhang, Z.; Chen, Q.; Zuo, C. Accurate quantitative phase imaging by differential phase contrast with partially coherent illumination: beyond weak object approximation. *Photonics Research* **2023**, *11*, 442–455.
- (17) Hamilton, D.; Sheppard, C.; Wilson, T. Improved imaging of phase gradients in scanning optical microscopy. *Journal of microscopy* **1984**, *135*, 275–286.
- (18) Streibl, N. Three-dimensional imaging by a microscope. *JOSA A* **1985**, *2*, 121–127.
- (19) Fischer, E. G. Nuclear morphology and the biology of cancer cells. *Acta cytologica* **2020**, *64*, 511–519.